CHALMERS
UNIVERSITY OF TECHNOLOGY

Role of molecular architecture and temperature on extrusion melt flow instabilities of two industrial LLDPE and LDPE polyethylenes investigated

Received: 27 June 2022 | Revised: 24 August 2022 | Accepted: 5 September 2022

DOI: 10.1002/app.53165

RESEARCH ARTICLE

Applied Polymer SCIENCE WILEY

Role of molecular architecture and temperature on extrusion melt flow instabilities of two industrial LLDPE and LDPE polyethylenes investigated by capillary rheology, high-pressure sensitivity slit die and optical analysis

Christos K. Georgantopoulos[1] | **Masood K. Esfahani**[1] | **Ingo F. C. Naue**[1] | **Manfred Wilhelm**[1] | **Roland Kádár**[2]

[1]Institute of Chemical Technology and Polymer Chemistry, Karlsruhe Institute of Technology (KIT), Karlsruhe, Germany

[2]Department of Industrial and Materials Science, Chalmers University of Technology, Gothenburg

Correspondence
Manfred Wilhelm, Institute of Chemical Technology and Polymer Chemistry, Karlsruhe Institute of Technology (KIT), Engesserstraße 18, 76131 Karlsruhe, Germany.
Email: manfred.wilhelm@kit.edu

Roland Kádár, Department of Industrial and Materials Science, Chalmers University of Technology, SE-412 96 Gothenburg, Sweden.
Email: roland.kadar@chalmers.se

Abstract

The characteristic time periodicity τ^* and the spatial characteristic wavelength λ of extrusion flow instabilities of a linear and a branched commercial polyethylene (PE) are characterized via capillary rheology, optical analysis and modeled. The two investigated polyethylenes have the similar weight average molecular weight (M_w). The characteristic time periodicity τ^* is obtained and compared using three methods: (i) a highly sensitive pressure slit die, (ii) a new online optical analysis method based on the construction of a space–time diagrams, and (iii) an offline transmission polarization microscopy. In addition, the spatial characteristic wavelength λ is quantified by offline transmission polarization microscopy. The characteristic time periodicity τ^* of the extrusion flow instabilities follows a power law behavior as a function of apparent shear rate to a power of −0.7 for both materials, $\tau^* \propto \dot{\gamma}_{app.}^{-0.7}$. A qualitative model is used to predict the spatial characteristic wavelength λ of extrusion flow instabilities as well. It is found that the characteristic spatial wavelength λ and the characteristic time periodicity τ^* have an Arrhenius temperature-dependent behavior.

KEYWORDS

extrusion instabilities, online optical analysis, polyethylene, sharkskin

1 | INTRODUCTION

Extrusion flow instabilities are a significant industrial problem, which appears at the die exit of numerous extrusion processes, for example, film blowing and film casting, and reduce mechanical and optical properties of the product.[1–7] Extrusion instabilities are in general categorized as surface and/or volume distortions.[5,8–10] Increasing extrusion throughput, usually, the smooth extrudate appearance has a transition to sharkskin first at low shear rates, then to stick–slip at medium shear rates, and last to gross melt fracture (GMF) at high shear rates. Definitions of the extrusion instabilities based on slit die geometry are discussed in the literature.[8–11] These

definitions are based on visual observations and on the characteristic frequency (or time periodicity) of the time dependent pressure signal obtained by a custom high pressure sensitive slit die (HPSSD).[8,9,11–25]

Sharkskin extrudates have a visual appearance characterized by superficial fractures perpendicular to the extrusion flow direction. Therefore, sharkskin is defined[8,9] as having small amplitude surface distortions, compared to the extrudate thickness, with one dominant characteristic distortion frequency, for example, in the literature $f_{Char.} \approx 20\,\text{Hz}$ for a specific linear low density polyethylene (LLDPE, $M_w = 193\,\text{kg mol}^{-1}$, $Đ = 9.65$) at $T = 140°\text{C}$,[13] and $f_{\text{Char.}} \approx 15\,\text{Hz}$ for a specific styrene–butadiene rubber (SBR, $M_w = 390\,\text{kg mol}^{-1}$, $Đ = 1.36$) at $T = 120°\text{C}$.[23] Conventional melt pressure transducers, commonly used in extrusion processing and on capillary rheometers, are not capable of capturing these high-frequency pressure fluctuations associated with the sharkskin instability.

Stick–slip instability is visually characterized by alternating smooth and/or sharkskin regimes in addition to irregular both surface and volume extrudate distortions. Stick–slip typically appears with pressure fluctuations of about $\Delta p/p \approx 25\%$ for $p \approx 200\,\text{bar}$ mean pressure[23] as determined by conventional melt pressure transducers on capillary rheometers. The stick–slip instability is typically characterized by at least three characteristic time periodicities (or frequencies): (i) one which occurred by the stick part, usually sharkskin instability, τ^*_{stick} with a typical value of $\tau^*_{stick} = 0.1$ s for a specific SBR rubber ($M_w = 390\,\text{kg mol}^{-1}$, $Đ = 1.36$) at $T = 120°\text{C}$,[23] (ii) one obtained by the slip part, usually volume distortion τ^*_{slip} with a typical value of $\tau^*_{\text{slip}} = 0.3$ s for a specific SBR rubber ($M_w = 390\,\text{kg mol}^{-1}$, $Đ = 1.36$) at $T = 120°\text{C}$,[23] and (iii) the last one obtained by the pressure fluctuations τ^*_{pressure} ($\Delta p/p \approx 25\%$ for $p \approx 200\,\text{bar}$) with a typical value of $\tau^*_{\text{pressure}} = 100\,\text{s}$.[23] Based on the recent findings[23] for SBR materials, these characteristic time periodicities are typically different to each other by $\tau^*_{\text{slip}} \approx 3\tau^*_{\text{stick}}$, and $\tau^*_{\text{pressure}} \approx 500\tau^*_{\text{stick}}$.

The last instability, gross melt fracture (GMF) is characterized by significant irregular distortions of the whole extrudate and therefore can be designated as a volume instability. No periodic pattern in space or time has been observed for the GMF.[10]

While the aforementioned instabilities are the most common and have been studied in a variety of linear and short-chain branched polymers such high-density polyethylene (HDPE), linear low-density polyethylene (LLDPE), there are also systems that differ in extrusion instability types and/or their succession with increasing shear rate.[16,17,24,25] For example, extrusion by slit dies for long-chain branched polymers, such as LDPE, are typically displaying smooth surface, then a transition which is characterized by surface undulations and then GMF without manifesting stick–slip instability.[17,25] The main difference between the sharkskin and surface undulation instabilities can be observed in Figure 1, with the surface undulations of the specific LDPE being larger, less uniform across the extrudate and do appear as surface cracks, in contrast to sharkskin.

Sharkskin presents a regular well-developed pattern in the extrusion direction and for the investigated LLDPE samples at $T = 160°\text{C}$ have a range of characteristics frequencies between $f_{\text{Char}} \approx 5-50\,\text{Hz}$ (time periodicities $\tau^* \approx 0.2–0.02\,\text{s}$) at a range of apparent shear rates $\dot{\gamma}_{\text{app}} = 20–300\,\text{s}^{-1}$. The undulation instability is usually[25] observed for the investigated LDPE samples and is characterized by a semi-regular pattern with characteristic frequencies at $T = 160°\text{C}$ between $f_{\text{Char.}} \approx 1.5-15\,\text{Hz}$ (time periodicities $\tau^* \approx 0.7\,\text{to}\,0.07\,\text{s}$) at range of apparent shear rate $\dot{\gamma}_{\text{app.}} = 20\,\text{to}\,300\,\text{s}^{-1}$ as observed within this study. It is noted that while linear and short-chain branched polymers have received a lot of attention, instabilities in branched polymers have been far less investigated. A spatial characteristic wavelength λ can be observed in both sharkskin and surface undulations, see Figure 1. Spatial

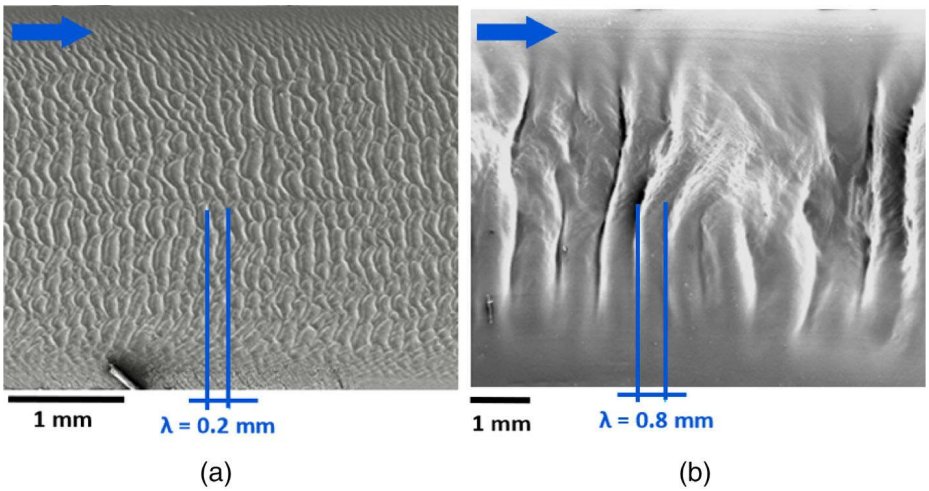

FIGURE 1 Scanning electron microscopy (SEM) of the surface of extrudates for (a) LLDPE ($M_w = 144$ kg Mol^{-1}, $Đ = 7.9$) and (b) LDPE ($M_w = 126$ kg Mol^{-1}, $Đ = 7.9$) at $\dot{\gamma}_{app.} = 100\,\text{s}^{-1}$ and $t = 160°\text{C}$. (a) Presents sharkskin for the LLDPE and (b) presents the undulation instability for the LDPE samples. The blue arrows indicate the extrusion direction. [Color figure can be viewed at wileyonlinelibrary.com]

characteristic wavelength λ is defined as the average distance between two similar consecutive distortions.[23]

The molecular origin of extrusion flow instabilities remains a topic of scientific debate.[1–7] Computational fluid dynamic (CFD) numerical simulations by Karapetsas and Tsamopoulos,[26] Pettas et al.,[27] Varchanis et al.[28] proposed that the origin of sharkskin instability is based on the extensional stress that a polymer chain experiences at the die exit in combination with its relaxation process shortly after leaving the die exit. Specifically, it is suggested[28] that the combination of the extensional thinning and the recoil state of the polymer chains in transient extensional flow at the die exit region and directly afterwards are the necessary conditions for the onset of the sharkskin instability. The rheological behavior of the extensional thinning and the characteristic time scale for the recovery of a macromolecular chain from a stretched to relaxed coil configuration is directly dependent on molecular properties, such as molecular weight and molecular architecture (linear, branching). Hence, these molecular properties can be responsible for the type of the surface instability. Indeed, by combining laser-Doppler velocimetry (LDV) with rheological experiments in both extension and shear, Burghelea et al.[29] compared the distributions of tensile and shear stresses in the extrusion flow of LLDPE ($M_w = 144\ \mathrm{kg\ mol^{-1}}$, $Đ = 7.9$) and LDPE ($M_w = 126\ \mathrm{kg\ mol^{-1}}$, $Đ = 7.9$). In contrast with the LLDPE, due to its long-chain branched structure, the LDPE was able to sustain higher tensile stresses prior to the onset of extrusion instability. Hence, the stress imbalance between the boundary layer and the bulk flow around the die exit resulted in a non-sharkskin instability for the LDPE sample. However, the LLDPE sample manifested a propagation of the extensional stress towards to the flow direction which resulted in a clear sharkskin pattern formation.[29] This highlights that the molecular properties determine the type of the surface instability on the extrudate based on the recent proposed theoretical concept.[28]

In addition to molecular properties, the impact of the processing parameters, such as the extrusion temperature, on the onset of the extrusion flow instabilities has been investigated as well. Plethora of studies[30–35] investigated the influence of temperature on the spatial and time characteristics of extrusion instabilities. The Arrhenius[6] temperature dependent behavior of the spatial characteristic wavelength λ and time periodicity τ^* of the flow instabilities for commercial LLDPE ($M_w = 112\ \mathrm{kg\ mol^{-1}}$, $Đ = 4.15$) sample has been reported by Wang et al.,[30,32] Barone et al.,[31] Furthermore, Miller et al.,[33,34] studied the influence of temperature on the spatial characteristic height h of extrusion flow instabilities for LLDPE ($M_w = 85\ \mathrm{kg\ mol^{-1}}$, $Đ = 2.30$) and reported an Arrhenius[6] temperature-dependent behavior as well. Georgantopoulos et al.[35] studied the influence of temperature on the spatial characteristic wavelength λ of extrusion instabilities for a commercial SBR ($M_w = 263\ \mathrm{kg\ mol^{-1}}$, $Đ = 1.67$) where the Arrhenius temperature dependent behavior of the wavelength for the SBR was validated as well.[35]

Within this study, three technics are used to characterize the extrusion flow instabilities of the investigated commercial PE samples. The characteristic time periodicity τ^* is obtained by the three different technics which have been recently validated for multiple industrial samples such as, high density, linear low density, and low-density polyethylene (HDPE, LLDPE, and LDPE), solution SBR, emulsion SBR, and rubber compounds samples.[8,9,11–25] The three different technics are: (i) a high-pressure-sensitive-slit die (HPSSD),[11–25] (ii) a new online optical analysis method based on the construction of space–time diagrams,[17,23] and (iii) an offline transmission polarization microscopy.[8,9,23] Secondly, the spatial characteristic wavelength λ, is quantified from offline transmission polarization microscopy. The characteristic time periodicities of the samples are evaluated as an extrusion "fingerprint" of the polymer molecular properties. Then, the validity of the power law behavior of the characteristic time periodicity as a function of shear rate and a modified[23] version of the model proposed by Wang et al.,[30] and Barone et al.,[31] for the spatial characteristic wavelength λ are discussed Moreover, the validity of the Arrhenius temperature-dependent behavior of the spatial and time characteristics of extrusion flow instabilities from the investigated samples is studied as well. Based on these three technics and the Arrhenius temperature-dependent behavior of the spatial and time characteristics of the extrusion instabilities four main questions with industrial importance will be answered: (1) which is the practical benefit for characterizing the extrusion instabilities based on the time characteristic?, (2) How many distinguishable time periodicities are developed during the extrusion process?, (3) Could the time characteristics identify the transitions from one type of extrusion instability to another?, and (4) which is the influence of extrusion temperature on the time characteristics of extrusion instabilities?

This study is an extension of the previous work[23] by our group where the similar online extrusion characterization technics are used.

2 | MATERIALS

Two industrial polyethylene samples with different molecular architectures are used in this study. The first is a LDPE, which has a molecular architecture consisting of random long-chain branches on branches. The second, is a linear LLDPE which has a linear backbone with short-chain

branches. High-temperature size exclusion chromatography (SEC) in combination with multiple-angle laser light scattering (MALLS) at $T = 140°C$ is used to molecularly characterize the investigated samples. The molecular weight distribution (MWD) of the samples is given in Figure 2 and their molecular and physical properties are listed in Table 1. Their common use is in the manufacturing of films through extrusion such as film casting and film blowing.

3 | CHARACTERIZATION TECHNIQUES

3.1 | Oscillatory shear rheology

Rheological experiments were carried out using a TA Instruments ARES-G2 (New Castle, DE, USA) strain-controlled rheometer. For the oscillatory frequency sweep experiments the rheometer was equipped with a plate-plate geometry, diameter of 13 mm. Small amplitude oscillatory shear (SAOS) frequency sweep tests were performed within $\gamma_0 = 1\% - 3\%$ constant strain amplitude in the linear viscoelastic (LVE) regime to obtain the magnitude of the complex viscosity, storage and loss moduli at $T = 140°C$, 160°C, and 180°C.

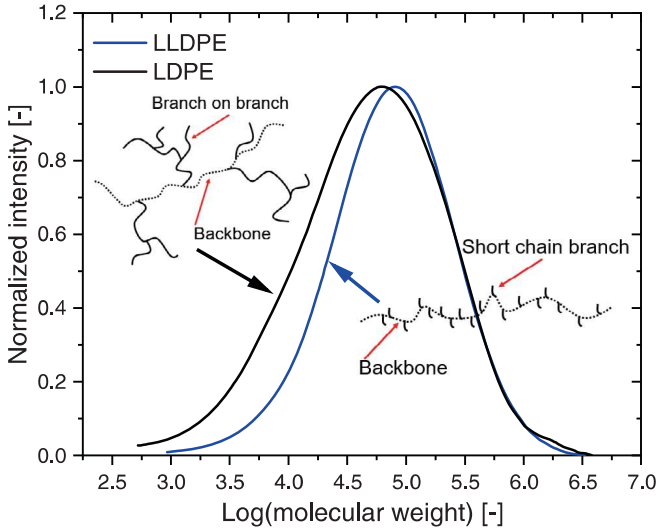

FIGURE 2 MWD of LDPE and LLDPE samples obtained by differential refractive index (DRI) detector. An idealized structure of the molecular architecture of each sample is presented as well. [Color figure can be viewed at wileyonlinelibrary.com]

TABLE 1 Physical and molecular properties of the investigated polymers

	LDPE	LLDPE
ρ (g cm^{-3}) at 25°C	0.919	0.926
ρ (g cm^{-3}) at 190°C[a]	0.760	0.760
T_m (°C)	110	125
M_w (kg mol^{-1})	126	144
$Đ$ (−)	7.9	4.4

[a]Text book value of melt bulk density for polyethylene samples at 190°C.[36]

3.2 | Capillary rheology

The samples were tested using a Göttfert Rheotester 2000 capillary rheometer (Buchen, Germany) equipped with a high sensitive pressure slit die system, Figure 3.[11–24] The extrusion slit die had a length of $L = 26$ mm and a rectangular cross-sectional area of 3×0.3 mm^2 ($W \times H$). Consequently, the aspect ratios were $W/H = 10$ and $L/H = 86.7$. Because the aspect ratio of $L/H > 60$, the pressure exits effect can be neglected.[36] Hence, the obtained apparent steady-state viscosity $\eta_{app.}$ (or apparent shear stress $\sigma_{app.}$) is the correct steady-state viscosity η (or wall shear stress σ_{wall}) without requiring a Bagley correction.[4,36] The slit die comprised a series of three highly sensitive piezoelectric (Kistler 6182CA) pressure transducers (Tr) distributed along the slit die. These were located, at 3 mm (Tr1), 13 mm (Tr2), and 23 mm (Tr3) from the die entrance, see Figure 3. The diameter of the piezoelectric pressure transducers is 2.5 mm. The transducer provides time and pressure resolutions after oversampling[37] of $\Delta t \approx 10^{-3}$ s and $\Delta p \approx 10^{-5}$ bar up to

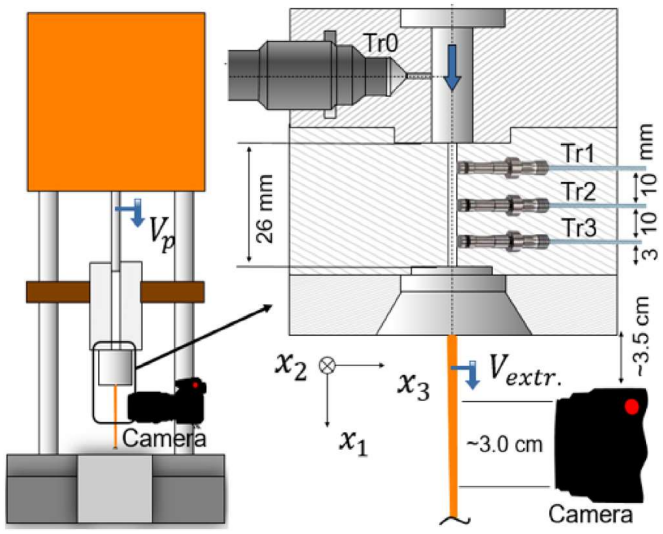

FIGURE 3 Schematic representation of the capillary rheometer and the highly pressure sensitive slit die. Marked transducers: Tr0—Conventional pressure transducer, Tr1—Tr3—Kistler (6182CA) highly sensitive piezoelectric pressure transducers. The ex-situ online optical visualization system (camera) was placed at a distance of ~3.5 cm below the die exit and ~3 cm from the extrudate surface. [Color figure can be viewed at wileyonlinelibrary.com]

nominal pressures of 2000 bar. The mechanical time-dependent pressure signal from the three piezoelectric transducers was further processed and then Fourier transformed. More details regarding the experimental system and time data processing can be found elsewhere.[8,9,22,23]

3.3 | Optical analysis of extrudates

Offline optical analysis of the solidified extrudates was carried out by transmission polarization microscopy at room temperature. Transmission polarization microscopy is a contrast-enhancing technique which uses polarizing filters, allowing the evaluation of the surface structure of the extrudate. A Zeiss Axiophot (Oberkochen, Germany) microscope is used in this study. The Zeiss Axiophot is equipped with two objectives of 2.5 and 10 magnification, and one ocular magnification of 10 times which resulted in an overall 25x and 100x magnification.

To monitor optical distortions at the die exit, before solidification ensues, an online optical system (camera) was incorporated in the capillary rheometer setup, see also Figure 3. The online optical monitoring has the advantages of avoiding extrudate distortions due to handling or thermal relaxation processes and does not require assumptions regarding the extrudate velocity. The methodology is explained below.[23] The online optical setup comprised a Canon 60D DSLR camera (Tokyo, Japan) as an online extrudate optical monitoring system. The camera was positioned ~3.5 cm below the die exit, perpendicular to the extrudate width (front view, $x_1 - x_2$, see Figure 3). A 100 mm Canon L-series macro lens combined with a 25 mm extension tube completed the optical setup, thus allowing appropriate magnification while positioned at a distance of ~3 cm from the extrudate. Full high-definition (1280 × 720 pixels) video recordings at 60 frames-per-second (fps) were acquired for ~5 minutes duration.

The video recordings were then used to construct space–time diagrams. The construction of a space–time diagrams has been presented in detail by Kádár[17] and Georgantopoulos et al.[23] In Figure 4, a brief description for the construction and application of the space–time diagram using the investigated LDPE sample is presented. From each video frame a line of pixels (px) at a constant position along x_1 (extrusion direction, see Figure 3) is extracted, Figure 4a, and then added to a newly created image, see Figure 4b. Thus, one axis corresponds to the width of the video frame, W_v, and the other axis to the experimental time, t. In Figure 4c an example of space–time diagram using the investigated LDPE sample is presented. Further image processing can be applied to correct for lateral drifts of the extrudate with reference to one of the edges, compare the bottom and the top versions, Figure 4c. The drift corrected space–time diagram allows for an easier extraction of grayscale intensity variations for long data sets and better identification of the characteristic time periodicity τ^*. The drift correction is implemented here for the first time due to intensive vibrations of the sample during extrusion. Georgantopoulos et al.[23] did not use the

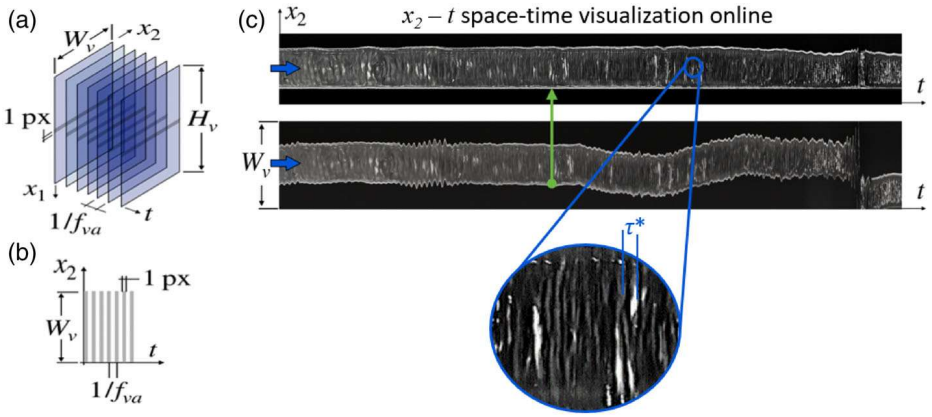

FIGURE 4 a–b. Sketch of the basic principle for the construction of space–time diagrams from a video with frame dimensions $W_v \times H_v$ and frame (acquisition) rate of f_{va}. (a) – (b) are adapted from Georgantopoulos et al.,[23] Figure 3a and b. (c) Examples of online $x_2 - t$ (see Figure 3 for the coordinate system) extrudate optical space–time diagram, including lateral drift correction. Moreover, an enlarged part of the space–time diagram indicates surface undulations and their characteristic time periodicity τ^*. The presented material is LDPE investigated at $T = 160°C$ and $\dot{\gamma}_{app.} = 100\,s^{-1}$, while the blue arrows indicate the extrusion direction. [Color figure can be viewed at wileyonlinelibrary.com]

drift correction since the development of extrusion instabilities appeared in smaller extrusion rates, and the width of the extrudates were almost twice as in the present work which allowed a better visualization. The characteristic time periodicity τ^*obtained by the online optical analysis setup is defined as the time between two consecutive similar events in the space–time diagram, see Figure 4c enlarged area.[23]

In Figure 5, the optical analysis of stick–slip instability of the investigate LLDPE is presented. Figure 5a presents an offline image of the stick–slip instability for comparison. The stick and slip part are indicated in the image. Figure 5b displays the space–time diagram of three stick–slip instabilities. Each part, stick and slip, has its own characteristic time periodicity τ^*_{stick} and τ^*_{slip}, respectively. The rapid slippage causes fluctuations on the whole extrudate and for this reason the space–time diagram demonstrates those three intensive oscillations, see left-hand-side enlarged indication in Figure 5b. During the stick part, pronounced sharkskin instability is manifested without intensive fluctuations during extrusion. The average characteristic time periodicity τ^* of the stick, τ^*_{stick} and slip, τ^*_{slip} part are mentioned on the right- and left-hand-side enlarged items in Figure 5b, respectively. In Figure 5c, the pressure oscillations which occurred during the recording of the video are presented. The pressure buildup represents the stick part and the rapid pressure drop the slip part. The pressure profile corresponds well to the space–time diagram in Figure 5b. It should also be noted that the slip part is larger in extrudate length than the stick part (see Figure 5a), however, slip part is shorter in time than the stick part (see Figure 5b). Therefore, the space–time diagram is an accurate representation of stick–slip dynamics in contrast to offline image analysis.

4 | MODELING

4.1 | Viscosity model

A Cross model,[38] Equation (1), is used to fit the magnitude of complex viscosity for each material, where η_0 is the zero-shear viscosity, τ is the longest characteristic relaxation time of the material and m is the shear-thinning exponent. The fitted parameters of the model are listed in Table 2.

$$|\eta(\omega)^*| = \frac{\eta_0}{1+(\tau\omega)^m}. \quad (1)$$

4.2 | Modeling of the spatial and time characteristics of flow instabilities

The spatial characteristic wavelength λ of the extrusion instabilities is defined as the average spatial distance between two consecutive similar distortions, see Figure 1.[23] Wang et al.,[30] and Barone et al.[31] mathematically described the wavelength as follows:

$$\lambda = \langle V \rangle \tau^*. \quad (2)$$

TABLE 2 Fitting parameters for the cross model, Equation (1) at $T = 160°C$.

Name	η_0 (kPa·s)	τ (s)	m (–)	E_a (kJ Mol^{-1})
LLDPE	21.5	0.25	0.6	31.0
LDPE	40	6	0.6	33.5

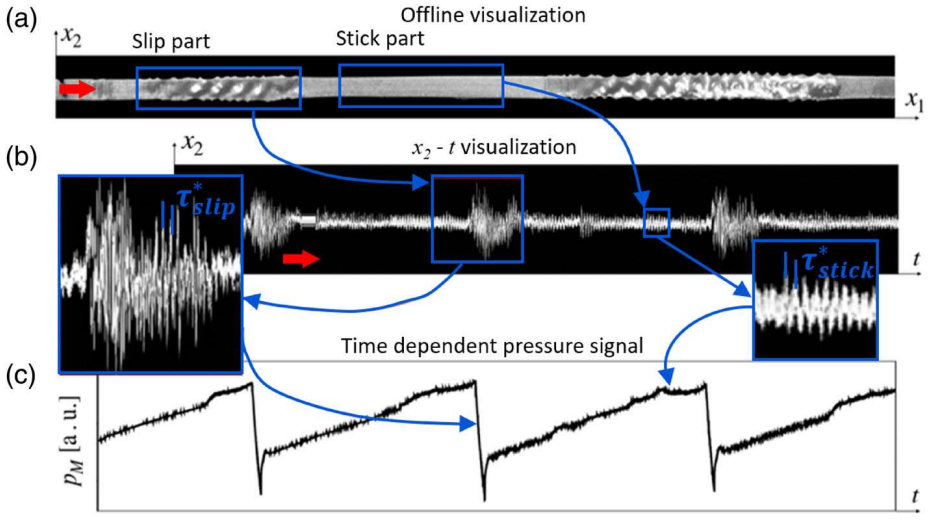

FIGURE 5 (a) Offline image of the stick–slip instability, where the stick and slip parts are mentioned in the blue frames. (b) Examples of an x_2 – T space–time visualization diagram for three stick slip instabilities; (c) associated mechanical time-dependent pressure fluctuations from one of the piezoelectric transducers. The material is the LLDPE investigated at $T = 160$ °C and $\dot{\gamma}_{app.} = 152\,s^{-1}$. The red arrows indicate the extrusion direction. [Color figure can be viewed at wileyonlinelibrary.com]

where $\langle V \rangle$ is the average extrudate velocity and $\tau^*$is the characteristic time periodicity of the extrusion flow instabilities. The average extrudate velocity for capillary dies (circular cross-section area) is given by

$$\langle V \rangle = V_{\text{extr.}}^{\text{Capillary}} (D/D')^2, \tag{3}$$

where $(D/D')^2$ is the swelling factor, D is the diameter of the die, and D' is the swelled diameter of the extrudate.[30–32] In addition, the average extrudate velocity for slit dies (rectangular cross-section area) is given by

$$\langle V \rangle = V_{\text{extr.}}^{\text{Slit}} \left(\frac{W}{W'} \frac{H}{H'} \right), \tag{4}$$

where $\left(\frac{W}{W'} \frac{H}{H'}\right)$ is the swelling factor, H is the height and W the width of the slit die, and H' and W' are the swelled dimensions of the extrudate.[23] The extrudate velocity of the capillary and slit dies are given by Equation (5) and (6), respectively,

$$V_{\text{extr.}}^{\text{Capillary}} = (D/8)\dot{\gamma}_{\text{app.}}, \tag{5}$$

$$V_{\text{extr.}}^{\text{Slit}} = (H/6)\dot{\gamma}_{\text{app.}}, \tag{6}$$

where $\dot{\gamma}_{\text{app.}}$ is the apparent shear rate.

Hence, coupling Equation (2), (4), and (6) the analytical expression for the spatial characteristic wavelength λ referring to slit die geometry is given by Equation (7).

$$\lambda^{\text{Slit}} = \frac{H}{6} \left(\frac{H}{H'} \frac{W}{W'} \right) \dot{\gamma}_{\text{app.}} \tau^*. \tag{7}$$

Following the simplification proposed by Georgantopoulos et al.,[23] it is assumed that $(H/H') \approx 1$. Hence, Equation (7) yields to Equation (8).

$$\lambda^{\text{Slit}} = \frac{H}{6} \left(\frac{W}{W'} \right) \dot{\gamma}_{\text{app.}} \tau^*. \tag{8}$$

Consistent with the recent findings from the present study and other similar works[18,23,39,40] the characteristic time periodicity τ^* of the flow instabilities can be simply described by a power law function of apparent shear rate $\dot{\gamma}_{\text{app.}}$

$$\tau^* = \frac{1}{f_{\text{Char.}}} = a\dot{\gamma}_{\text{app.}}^{\ -b}, \tag{9}$$

where a and b are constants and assumed to be material dependent.[18,23,39,40]

The characteristic time periodicity τ^* is here obtained by three different techniques. Firstly, by the Fourier transformation of the already processed time-dependent pressure data by the three piezoelectric pressure transducers obtained by the HPSSD,[8,9,11–25] $\tau^*_{\text{FT pressure}}$. The $\tau^*_{\text{FT pressure}}$ is obtained by the pressure signal which is recorded inside the HPSSD; hence, it requires swelling ratio correction according to Equations (2) and (4). Secondly, the time periodicity obtained by the online optical analysis technique which monitors the already swelled extrudate, $\tau^*_{\text{online optical}}$ and does not need swelling correction. Lastly, from offline optical analysis the time periodicity $\tau^*_{\text{offline optical}}$ is calculated from the ratio of the spatial characteristic wavelength λ, with the extrudate velocity $V_{\text{extr.}}^{\text{Slit}}$ (Equation (6)) and the swelling ratio (W/W').

5 | RESULTS AND DISCUSSION

5.1 | Rheological properties

Capillary rheology experiments were carried out at three different temperatures $T = 140°C$, 160°C, and 180°C with the highly pressure sensitive slit die ($H = 0.3$ mm, $W = 3$ mm, and $L = 26$ mm) for both samples. The wall shear stress as a function of apparent shear rate for both materials investigated at the three temperatures is plotted in Figure 6. As expected based on their molecular architecture, the LLDPE flow curves are non-monotonic, while LDPE are monotonic.[10] The wall shear stress is generally inversely proportional to the temperature for both materials. However, for the LLDPE sample between $\dot{\gamma}_{\text{app.}} = 100$ and $700\,\text{s}^{-1}$ an opposite trend is observed. At

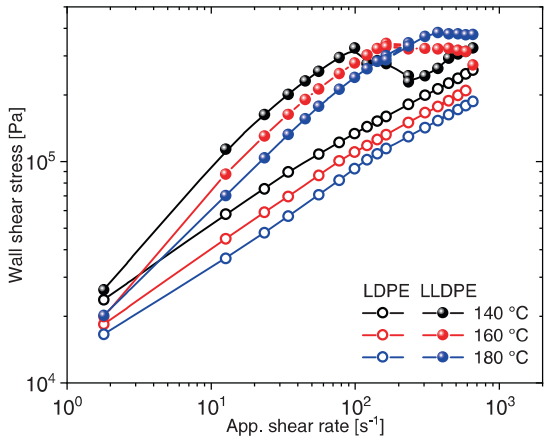

FIGURE 6 Wall shear stress as a function of the apparent shear rate obtained by capillary rheology with a slit die $H = 0.3$ mm, $W = 3$ mm and $L = 26$ mm. Both LDPE and LLDPE have been investigated at $T = 140°C$, 160°C, and 180°C. [Color figure can be viewed at wileyonlinelibrary.com]

$T = 140°C$, a stick–slip instability exists between $100 < \dot{\gamma}_{app.} < 250\,s^{-1}$ and a negative slope in the wall shear stress is observed. At $T = 160°C$, the stick–slip instability appeared at $\dot{\gamma}_{app.} = 130\,s^{-1}$ until $\dot{\gamma}_{app.} \approx 270\,s^{-1}$ followed by gross melt fracture (GMF). At $T = 180°C$, stick–slip instability appears at $\dot{\gamma}_{app.} \approx 270\,s^{-1}$ followed by GMF. The lower values of the wall shear stress, despite the lower temperatures, were therefore caused by the intensive slippage after the appearance of stick–slip instability, and for this reason the stress is underestimated.[10]

In Figure 7, the master curve of the magnitude of complex viscosity as a function of angular frequency at $T = 160°C$ as reference temperature is presented. Additionally, the steady-state viscosity as a function of apparent shear rate at $T = 160°C$ is overlaid in the same plot. Therefore, the applicability of the Cox–Merz rule[41] empirical relationship is verified within the experimental window. The Cox–Merz rule relates the linear oscillatory shear with the nonlinear steady-state shear data. Hence, it states that the shear rate dependency of the steady-state viscosity $\eta(\dot{\gamma})$ is equal to the magnitude of the complex viscosity $|\eta^*(\omega)|$, that is, $\eta(\dot{\gamma}) = |\eta^*(\omega)|$, with the magnitude values of $\dot{\gamma} = \omega$.[41] The Cox–Merz rule[41] applicability relies on the assumptions of the validity for linear monodisperse homopolymer melt. Although Cox–Merz rule has been verified experimentally for many different materials such as styrene–butadiene rubbers, polycaprolactones, polyethylene, and polystyrenes.[23,35,42]

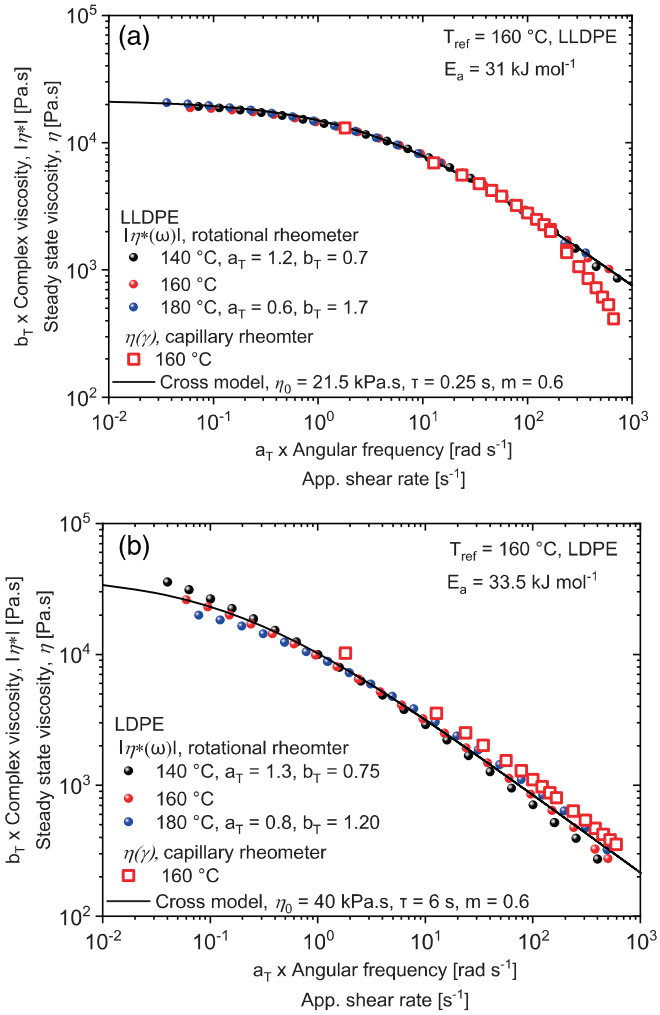

FIGURE 7 Master curve of the magnitude of the complex viscosity as a function of angular frequency at reference temperature of $T = 160\,°C$ for (a) LLDPE and (b) LDPE. Steady-state viscosity as a function of apparent shear rate obtained at $T = 160\,°C$ as well. the experimental results of the magnitude of complex viscosity are fitted by cross model (Equation (1)). [Color figure can be viewed at wileyonlinelibrary.com]

Ansari et al.[42] and Ebrahimi et al.[43] observed that the Cox-Merz rule is valid for broad MWD high-density polyethylene (HDPE) with a dispersity index $Đ < 15$ at $T = 190°C$. Figure 7 (a) presents agreement of the Cox–Merz rule for the LLDPE sample at $T = 160°C$ between $\dot{\gamma}_{app.} = 2$ and $130\,s - 1$. Failure of the Cox–Merz rule is observed at $\dot{\gamma}_{app.} > 130\,s^{-1}$ and is caused by the intensive slippage due to the onset of stick–slip and GMF instabilities, as discussed ahead. For this reason, the steady-state viscosity has apparent lower values than the magnitude of the complex viscosity.[42,43] For the LDPE, Figure 7b, the Cox–Merz rule fails in the whole region of measurement. The experimental data are fitted by the Cross model, Equation (1), and the fitting parameters are listed in Table 2.

5.2 | Extrudate velocity evaluation

To evaluate the validity of Equation (4) which is commonly used in the literature,[23,30–32,35,44] experimental results from the online optical analysis are presented in Figure 8. In Figure 8, the extrudate velocity $V^{Slit}_{extr.}$ obtained by Equation (6) and the average extrudate velocity $\langle V \rangle$ obtained by the online optical analysis are presented. The $\langle V \rangle$ is calculated from Equation (2) using $\tau^*_{online\ optical}$. According to Equation (4), the difference between the two velocities is the swelling ratio $\left(\frac{W}{W'}\frac{H}{H'}\right)$. The term (H/H') is assumed to be 1.[23] The swelled width W' of the samples is measured from the collected extrudates after the extrusion at room temperature. Hence, on average the swelling ratio at $T = 160°C$ for the LDPE is $(W/W') \approx 0.61$ and for LLDPE is $(W/W') \approx 0.65$. Based on the experimental data (Figure 8), the $V^{Slit}_{extr.}$ is higher than $\langle V \rangle$ by a factor ~ 0.5 which is similar to the swelling ratio for both samples. Deviation between the ~ 0.5 factor and the absolute value of the average swelling factors (for LDPE $(W/W') \approx 0.61$ and for LLDPE $(W/W') \approx 0.65$) is possibly occurs due to difficulties to precisely measure the swelled width W' and the assumption of $(H/H') \approx 1$.[23]

5.3 | Identifying the main instability type

In Figures 9 and 10 space–time diagrams of the LLDPE and LDPE are presented, respectively. Indeed, in Figure 9, a sharkskin instability at $\dot{\gamma}_{app.} = 100\,s^{-1}$ and $T = 160°C$ and in Figure 9b stick–slip instability at $\dot{\gamma}_{app.} = 159\,s^{-1}$ and $T = 160°C$ of the LLDPE sample are presented. In Figure 9b, two characteristic time periodicities are mentioned $\tau^*_{stick} = 0.03\,s$ and $\tau^*_{slip} = 0.1\,s$, and indeed the ratio between them is $\tau^*_{stick}/\tau^*_{slip} \approx 3$.[23] The ratio of 3 between τ^*_{stick} and τ^*_{slip} has also been observed for SBR materials as well.[23]

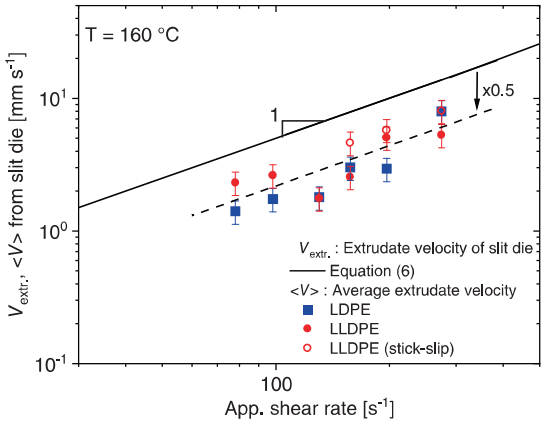

FIGURE 8 Extrudate velocity $V^{Slit}_{extr.}$ and average extrudate velocity $\langle V \rangle$ as a function of apparent shear rate. The $V^{Slit}_{extr.}$ is computed from Equation (6) and $\langle V \rangle$ is obtained by the online optical system for both materials. The $V^{Slit}_{extr.}$ is higher than $\langle V \rangle$ by a factor ~0.5 which is similar to the swelling ratio. [Color figure can be viewed at wileyonlinelibrary.com]

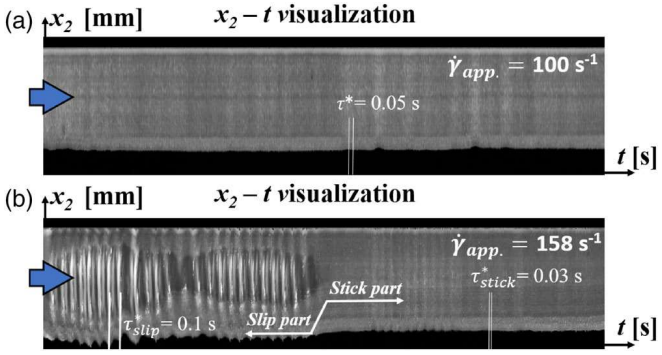

FIGURE 9 Space–time diagram of the LLDPE at $T = 160°C$ for two different apparent shear rates. (a) Sharkskin instability at $\dot{\gamma}_{app.} = 100\,s^{-1}$ and (b) stick–slip instability at $\dot{\gamma}_{app.} = 158\,s^{-1}$. The characteristic time periodicity is mentioned in the diagram. The (b) has two characteristic time periodicities and each one represents the stick and the slip part of the stick–slip instability. The blue arrows show the extrusion direction. The time scale between (a) and (b) is not the same, although they have the similar length for visualization purposes. [Color figure can be viewed at wileyonlinelibrary.com]

In Figure 10 the space–time diagrams of the LDPE at $\dot{\gamma}_{app.} = 78\,s^{-1}$ and $\dot{\gamma}_{app.} = 130\,s^{-1}$ are presenting the surface undulation instability and its characteristic time periodicity. One characteristic time periodicity can be found in those space–time diagrams at $T = 160°C$. Using the online optical visualization analysis the difference in the time characteristics and in the type of extrusion instabilities can easily be observed, comparing Figures 9 and 10. It is noted here that the in-situ pressure and ex-situ optical evaluations are in contrast to the observations of Burghelea et al.[29] where the LDPE sample was considered as a "no sharkskin" reference sample. While the present data concurs that the LDPE does not manifest sharkskin instability, the surface of the extrudate has undulations which are distinct for polymers with long-chain branches.[16,17,24,25]

5.4 | Characteristic time periodicity

The characteristic time periodicity τ^* was obtained using three different techniques: (i) a high-pressure-sensitive-slit die (HPSSD)[11–25] with height $H = 0.3\,mm$, width $W = 3\,mm$ and length $L = 26\,mm$, (ii) a new online optical analysis method based on the construction of a space–time diagram,[17,23] and (iii) an offline transmission polarization microscopy.[8,9,23,35] It is noted that the melt flow instabilities might have more than one characteristic time periodicity e.g. at least three have been previously identified for the stick–slip instability.[16,17,23] This study is focusing on the dominant characteristic frequencies on the surface of the extrudate for the stick–slip instability, that is, τ^*_{stick} for the stick part, and τ^*_{slip} for the slip part.

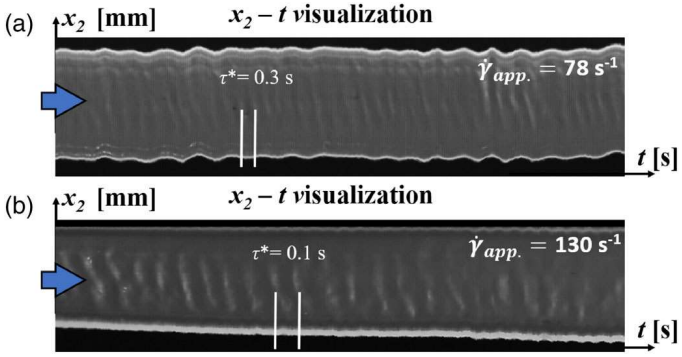

FIGURE 10 Space–time diagram of the LDPE at $T = 160°C$ for two different apparent shear rates, (a) at $\dot{\gamma}_{app.} = 78\,s^{-1}$ and (b) at $\dot{\gamma}_{app.} = 130\,s^{-1}$. The extrusion instability is characterized as surface undulation instability and one characteristic time periodicity is observed. the blue arrows show the extrusion direction. The time scale between (a) and (b) is not the same, although they have the similar length for visualization purposes. [Color figure can be viewed at wileyonlinelibrary.com]

Consequently, the characteristic time periodicities associated with the pressure fluctuation during the stick–slip instability are neglected. The characteristic time periodicities obtained by the HPSSD $\tau^*_{\text{FT pressure}}$, the online optical analysis technique $\tau^*_{\text{online optical}}$ and the offline optical analysis $\tau^*_{\text{offline optical}}$ are compared in Figure 11 for both materials. The $\tau^*_{\text{FT pressure}}$ and $\tau^*_{\text{online optical}}$ obtained at $T = 160°C$, and the master-curve of the $\tau^*_{\text{offline optical}}$ developed by three temperatures, $T = 140°C$, $160°C$, and $180°C$, at reference temperature of $T = 160°C$ is therein presented. The shift factors a_T and b_T used to shift the data of the characteristic time periodicity $\tau^*_{\text{offline optical}}$ are similar to the shift factors from the master-curve of the magnitude of complex viscosity for both materials, see Figure 7. For the LLDPE, Figure 7a, two characteristic time periodicities are observed after the onset of stick–slip instability the τ^*_{stick} and τ^*_{slip}. Moreover, the ratio of the characteristic time periodicity from stick and slip part of the stick–slip instability is $\tau^*_{\text{stick}} \approx 2.4 \cdot \tau^*_{\text{slip}}$ which is similar to the ratio previously reported by Georgantopoulos et al.[23] for SBR. The obtained characteristic time periodicities from the three different techniques are fitted by the power law function, Equation (9), and the overall deviation of each technique from the fitting function is estimated to vary at most by 20%. The power law function which describes the experimental data for both materials is $\tau^* = 1.3\dot{\gamma}^{-0.7}_{\text{app.}}$ for the LLDPE and $\tau^* = 5.2\dot{\gamma}^{-0.7}_{\text{app.}}$ for the LDPE. The slope of the characteristic time periodicity as a function of apparent shear rate for both materials remains the same at -0.7. The prefactor, which has been assumed to be material dependent, differs between the two investigated samples by a factor 4 (1.3 for LLDPE and 5.2 for LDPE). The investigated materials have the similar weight-averaged molecular weight (see Table 1) and they are extrudated by the same slit die, hence the prefactor might be related to molecular properties such as the molecular architecture and/or MWD rather than the weight average molecular weight (M_w). Similar findings have been presented in a previous study by our group[23] where two commercial SBR materials, with almost the same MWD and M_w but slightly different molecular architectures where extruded by the same die at $T = 120°C$. The SBR B was slightly more branched than the SBR A.[23] The characteristic time periodicity followed a power law behavior $\tau^* = 0.5\dot{\gamma}^{-0.5}_{\text{app.}}$ for SBR A and $\tau^* = 0.9\dot{\gamma}^{-0.5}_{\text{app.}}$ for SBR B. The slope of the characteristic time periodicity for both materials remains the same at -0.5 and the prefactor differs between the investigated SBR samples by a factor ~ 1.6 (1.5 for SBR A and 0.9 for SBR B).

The difference in the power law behavior of the characteristic time periodicity between the two set of investigated materials, PE and SBR, is the exponent, b, being -0.7 for PE and -0.5 for SBR. According to this, the rubbery materials manifest a faster type of surface fracture than the polyolefin materials under the same apparent shear rate based on those investigated samples. In addition, based on the current findings and those in literature[23] the pre-factor of the power law behavior of the characteristic time periodicity, Equation (9), is suggested to be related to molecular architecture (linear, branched) of the investigated sample.

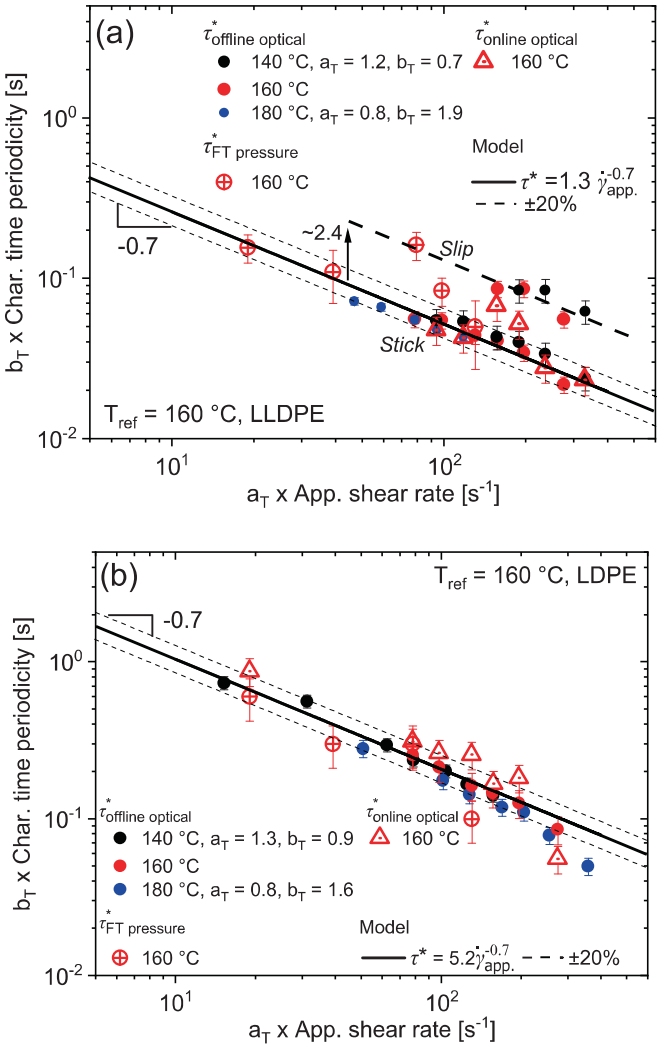

FIGURE 11 The master curve of the characteristic time periodicity as a function of apparent shear rate for (a) LLDPE and (b) LDPE at reference temperature of $T = 160\ °C$. all of the characteristic time periodicities $\tau^*_{\text{FT pressure}}$, $\tau^*_{\text{online optical}}$, and $\tau^*_{\text{offline optical}}$ are compared to each other and fitted by the power law model, Equation (9). [Color figure can be viewed at wileyonlinelibrary.com]

5.5 | Characteristic wavelength

The spatial characteristic wavelength λ of the extrusion flow instabilities is quantified by transmission polarization microscopy. The master-curves of the spatial

characteristic wavelength λ for both investigated materials at the reference temperature $T = 160\,^{\circ}\mathrm{C}$ are presented in Figure 12. For the developing of the master-curve the shift factors, a_T and b_T, obtained by the linear rheology are successfully applied on the spatial characteristic wavelength λ as well. The LLDPE sample in Figure 12 (a) presents two spatial characteristic wavelengths between $\dot{\gamma}_{app.} = 130\,s^{-1}$ and $275\,s^{-1}$ which indicates stick–slip instability. Offline optical analysis of the LLDPE at stick–slip instability are presented in Figure 13a. Each part, that is the stick and slip part, is characterized by its own spatial characteristic wavelength. It is observed that the wavelength obtained by the slip part is ~2.4 times larger than the wavelength obtained by the stick part, see Figure 12a. In Figure 12b, the spatial characteristic wavelength of the LDPE sample is presented and selected offline images are displayed in Figure 13b. The swelling ratios for both materials are $(W/W') \approx 0.61$ and $(W/W') \approx 0.65$ for LDPE and LLDPE at $T = 160^{\circ}\mathrm{C}$, respectively. In addition, for the characteristic time periodicity the power law functions from Figure 9 are used in order to predict the master-curve of the spatial characteristic wavelength for both materials by using Equation (8) at $T = 160^{\circ}\mathrm{C}$. The agreement between the prediction of Equation (8) and experimental data are observed in Figure 12.

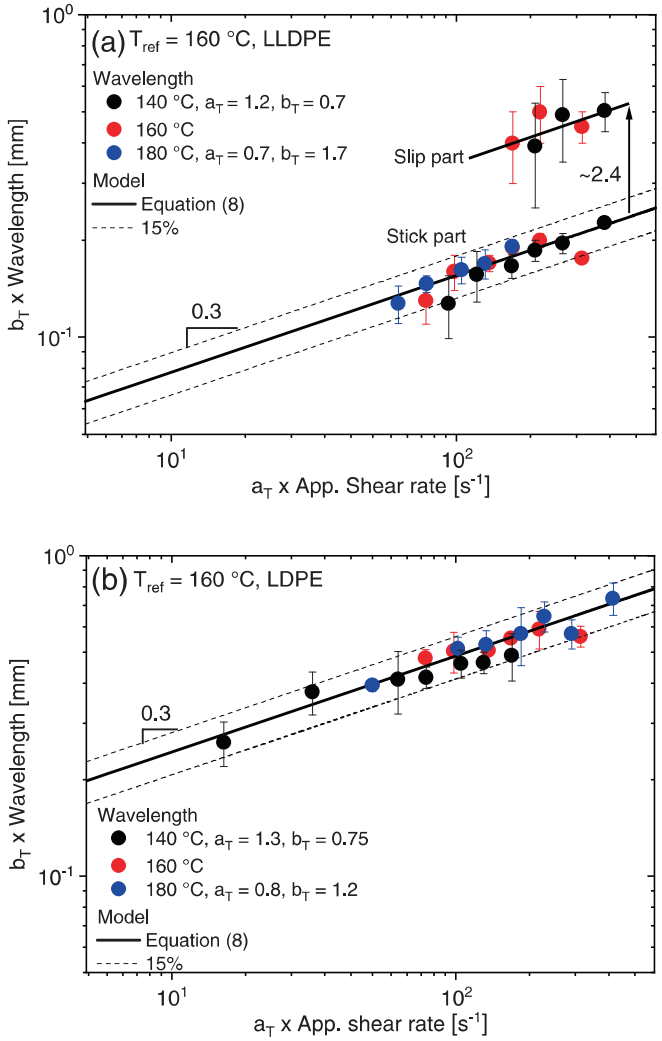

FIGURE 12 Master-curves of the spatial characteristic wavelength as a function of apparent shear rate for (a) LLDPE and (b) LDPE at reference temperature of $T = 160^{\circ}\mathrm{C}$. the spatial characteristic wavelength is obtained by the offline optical analysis. [Color figure can be viewed at wileyonlinelibrary.com]

6 | CONCLUSIONS

In this work, four main questions have been addressed regarding extrusion melt flow instabilities for a linear/short-chain branched LLDPE and a long-chain branched LDPE:

1. Which is the practical benefit for characterizing the extrusion instabilities based on the time characteristic?
2. How many distinguishable time periodicities are developed during the extrusion process?
3. Could the time characteristics identify the transitions from one type of extrusion instability to another?

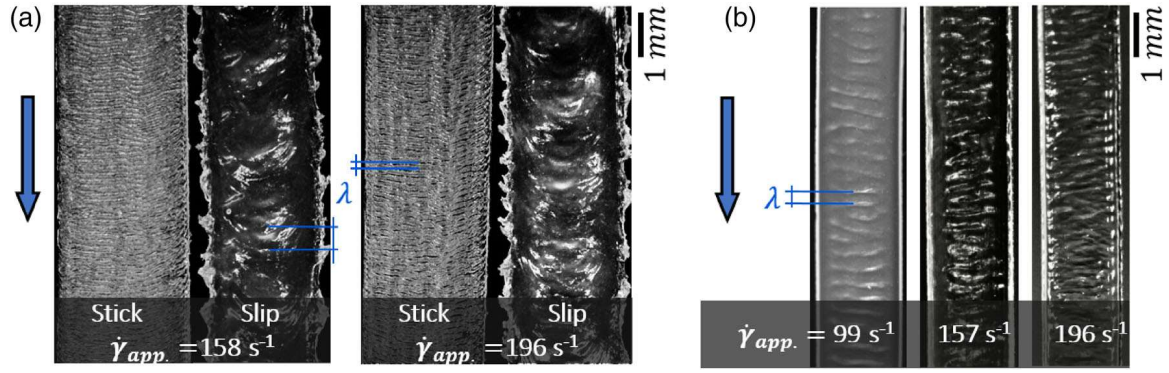

FIGURE 13 Offline optical analysis of (a) LLDPE and (b) LDPE investigated at $T = 160^{\circ}\mathrm{C}$. in (a) the stick and slip part are separately investigated. The blue arrow indicates the flow direction. [Color figure can be viewed at wileyonlinelibrary.com]

4. Which is the influence of extrusion temperature on the time characteristics of extrusion instabilities?

The in-situ observations provide information which can be used in order to determine instability parameters. Hence, based on the obtained results, the following conclusions have been drawn for the characterization and modeling of the time and spatial characteristics of extrusion flow instabilities for the investigated PE samples.

1. The characteristic time periodicity obtained by the three different techniques (highly pressure-sensitive slit die, space–time visualization and offline optical analysis) were in quantitative agreement and varied at most 20% from the fitting power law function (Equation (9)) for both samples.
2. The characteristic time periodicity as a function of apparent shear rate is described by Equation (9). The scaling exponent is −0.7 for both materials and the pre-factor deviates by a factor 4 between them. The investigated materials have the similar weight average molecular weight (see Table 1) and they are extruded by the same slit die, hence the prefactor might be related to molecular properties such as the molecular architecture rather than the weight average molecular weight (M_w).
3. The dominant spatial characteristic wavelengths of both materials are predicted by Equation (8), that is the modified qualitative model[13] of Wang et al.[30] and Barone et al.[31] The prediction of Equation (8) agrees with the experimental data.
4. The characteristic time periodicity τ^* and the spatial characteristic wavelength λ of flow instabilities follow an Arrhenius temperature-dependent behavior for the investigated samples. The shift factors a_T and b_T which are used to shift the data of the characteristic time periodicity τ^* and the spatial characteristic wavelength λ are similar to the shift factors obtained from the master-curve of the magnitude of complex viscosity for both materials. The activation energy of the materials are $E_a = 31\,\mathrm{kJ\,mol^{-1}}$ for LLDPE and $E_a = 33.5\,\mathrm{kJ\,mol^{-1}}$ for the LDPE.

AUTHOR CONTRIBUTIONS

Christos K. Georgantopoulos: Conceptualization (lead); data curation (lead); formal analysis (lead); investigation (lead); writing – original draft (lead). **Masood K. Esfahani:** Conceptualization (supporting); data curation (supporting); formal analysis (supporting). **Ingo F. C. Naue:** Conceptualization (supporting); data curation (supporting); formal analysis (supporting). **Roland Kádár:** Conceptualization (lead); data curation (lead); formal analysis (lead); supervision (lead). **Manfred Wilhelm:** Supervision (lead).

ACKNOWLEDGMENTS

The authors would like to acknowledge Prof. Dr. Markus Busch and Ms. Elisabeth Schulz for their help to perform and analyze the high-temperature SEC experiments for the polyethylene samples. Moreover, Prof. Dr. Helmut Münstedt is acknowledged for supporting us with scientific discussions and sample donation. The authors are thankful to Dr. Christopher Klein for a kind introduction to the microscope, Dr. Michael Pollard for proofreading the manuscript, and Dr. Andrea Causa for useful discussions. The authors would like to acknowledge Pirelli Tyres S. p. A. and DFG WI 1911/14-1 for financial support. Open Access funding enabled and organized by Projekt DEAL.

DATA AVAILABILITY STATEMENT

The data that support the findings of this study are available from the corresponding author upon reasonable request.

ORCID

Manfred Wilhelm https://orcid.org/0000-0003-2105-6946

REFERENCES

[1] A. Leonov, A. Prokunin, *Nonlinear Phenomena in Flows of Viscoelastic Polymer Fluids*, Chapman & Hall, London **1994**.
[2] M. M. Denn, *Ann. Rev. Fluid Mech.* **2001**, *33*, 265.
[3] S. G. Hatzikiriakos, *Prog. Polym. Sci.* **2012**, *37*, 624.
[4] S. G. Hatzikiriakos, K. Migler, *Polymer Processing Instabilities. Control and Understanding*, Marcel Dekker, New York **2005**.
[5] R. Koopmans, C. F. J. den Doelder, J. Molenaar, *Polymer Melt Fracture*, CRC Press, Boca Raton **2011**.
[6] S. Q. Wang, *Nonlinear Polymer Rheology: Macroscopic Phenomenology and Molecular Foundation*, John Wiley & Sons, New York **2017**.
[7] S. Q. Wang, in *Polymers in Confined Environments*, Vol. 1 (Eds: S. Granick, K. Binder, P. G. de Gennes, E. P. Giannelis, G. S. Grest, H. Hervet, R. Krishnamoorti, L. Léger, E. Manias, E. Raphaël, S. Q. Wang), Springer-Verlag, Berlin **1999**, Ch. 6.
[8] I. F. C. Naue, *Development of Improved Rheometric Tools and Their Application on the Non-Newtonian Rheology of Polymeric Fluids*, PhD Thesis, Karlsruhe Institute of Technology (KIT), Karlsruhe, Germany **2013**.
[9] I. F. C. Naue, R. Kádár, M. Wilhelm, *Macromol. Mater. Eng.* **2015**, *300*, 1141.
[10] C. F. J. den Doelder, *Design and Implementation of Polymer Melt Fracture Models*, PhD Thesis, Eindhoven University of Technology, Eindhoven, Netherlands, **1999**.
[11] A. Gansen, M. Řehoř, C. Sill, P. Polińska, S. Westermann, J. Dheur, J. S. Hale, J. Balle, *J. Appl. Polym. Sci.* **2020**, *137*, 48806.
[12] S. Filipe, A. Becker, V. C. Barroso, M. Wilhelm, *Appl. Rheol.* **2009**, *19*, 23345.

[13] H. Palza, I. F. C. Naue, M. Wilhelm, *Macromol. Rapid Commun.* **2009**, *30*, 1799.
[14] H. Palza, I. F. C. Naue, S. Filipe, A. Becker, J. Sunder, A. Göttfert, M. Wilhelm, *Kautsch. Gummi Kunstf.* **2010**, *63*, 456.
[15] H. Palza, B. Reznik, M. Kappes, F. Hennrich, I. F. C. Naue, M. Wilhelm, *Polymer* **2010**, *51*, 3753.
[16] R. Kádár, I. F. C. Naue, M. Wilhelm, *Polymer* **2016**, *104*, 193.
[17] R. Kádár, *Annu. Trans. Nordic Rheol. Soc.* **2017**, *25*, 191.
[18] C. K. Georgantopoulos, I. F. C. Naue, A. Causa, L. Garro, M. Wilhelm, *Annu. Trans. Nordic Rheol. Soc.* **2019**, *27*, 151.
[19] M. Barczewski, R. Barczewski, T. Chwalczuk, *J. Manuf. Process* **2020**, *59*, 153.
[20] M. Barczewski, R. Barczewski, T. Sterzynski, *J. Polym. Eng.* **2012**, *32*, 335.
[21] F. Cyriac, J. A. Covas, L. Hilliou, I. Vittorias, *Rheo. Acta* **2014**, *53*, 817.
[22] H. Palza, S. Filipe, I. F. C. Naue, M. Wilhelm, *Polymer* **2010**, *51*, 522.
[23] C. K. Georgantopoulos, M. K. Esfahani, C. Botha, I. F. C. Naue, N. Dingenouts, A. Causa, R. Kádár, M. Wilhelm, *Macromol. Mater. Eng.* **2021**, *306*, 2000801.
[24] R. Kádár, I. F. C. Naue, M. Wilhelm, *Annu. Trans. Nordic Rheol. Soc.* **2014**, *22*, 153.
[25] R. Kádár, *The Instability Book: a Gallery of Polymer Melt Extrusion Instabilities*, Apple Books, Minnesota **2014**. Epub ahead of print.
[26] G. Karapetsas, J. Tsamopoulos, *Phys. Fluids* **2013**, *25*, 93105.
[27] D. Pettas, G. Karapetsas, Y. Dimakopoulos, J. Tsamopoulos, *J. Non-Newtonian Fluid Mech.* **2015**, *224*, 61.
[28] S. Varchanis, D. Pettas, Y. Dimakopoulos, J. Tsamopoulos, *Phys. Rew. Lett.* **2021**, *8*, 88001.
[29] T. I. Burghelea, H. J. Griess, H. Münstedt, *J. Non-Newtonian Fluid Mech.* **2010**, *165*, 1093.
[30] S. Q. Wang, P. A. Drda, Y. W. Inn, *J. Rheol.* **1996**, *40*, 875.
[31] J. R. Barone, N. Plucktaveesak, S. Q. Wang, *J. Rheol.* **1998**, *42*, 813.
[32] S. Q. Wang, P. A. Drda, *Macromol. Chem. Phys.* **1997**, *198*, 673.
[33] E. Miller, J. P. Rothstein, *Rheo. Acta* **2004**, *44*, 160.
[34] E. Miller, S. J. Lee, J. P. Rothstein, *Rheo. Acta* **2006**, *45*, 943.
[35] C. K. Georgantopoulos, M. K. Esfahani, C. Botha, M. A. Pollard, I. F. C. Naue, A. Causa, R. Kádár, M. Wilhelm, *Phys. Fluids* **2021**, *33*, 093108.
[36] J. M. Dealy, J. Wang, *Melt Rheology and its Application in the Plastic Industry*, 2nd ed., Spingel Science + Business Media Dordrecht, Netherland **2013**.
[37] D. van Dusschoten, M. Wilhelm, *Rheol. Acta* **2001**, *50*, 395.
[38] F. A. Morrison, *Understanding Rheology*, Oxford University Press, Oxford **2001**.
[39] Y. W. Inn, L. Wang, M. T. Shaw, *Macromol. Symp.* **2000**, *158*, 65.
[40] J. R. Barone, S. Q. Wang, Paper IR6, SoR 70th Annual Meeting, **1998**.
[41] P. Cox, E. H. Merz, *J. Polym. Sci.* **1958**, *28*, 619.
[42] M. Ansari, S. G. Hatzikiriakos, A. M. Sukhadia, D. C. Rohlfing, *Rheol. Acta* **2011**, *50*, 17.
[43] M. Ebrahimi, T. Tomkovic, G. Liu, A. Doufas, S. G. Hatzikiriakos, *Phys. Fluids* **2018**, *30*, 53103.
[44] Y. W. Inn, R. J. Fisher, M. T. Shaw, *Rheol. Acta* **1998**, *37*, 573.

How to cite this article: C. K. Georgantopoulos, M. K. Esfahani, I. F. C. Naue, M. Wilhelm, R. Kádár, *J. Appl. Polym. Sci.* **2022**, e53165. https://doi.org/10.1002/app.53165